Journal of Hazardous Materials 194 (2011) 144–155

Contents lists available at ScienceDirect

Journal of Hazardous Materials

journal homepage: www.elsevier.com/locate/jhazmat

# Catalytic $NO_x$ removal by single-wall carbon nanotube-supported Rh nanoparticles

Eleni C. Vermisoglou*, George E. Romanos*, Georgios N. Karanikolos, Nick K. Kanellopoulos

*Institute of Physical Chemistry, Demokritos National Center for Scientific Research, Athens 153 10, Greece*

ARTICLE INFO

*Article history:*
Received 28 March 2011
Received in revised form 20 July 2011
Accepted 22 July 2011
Available online 5 August 2011

*Keywords:*
$NO_x$
Air pollution
Catalysis
SWNTs
PEG
Rhodium

ABSTRACT

Single-wall carbon nanotubes functionalized with polyethylene glycol and doped with Rh nanoparticles were prepared and tested as catalyst for $NO_x$ reduction. Gravimetric adsorption studies were employed to elucidate the mechanism of NO adsorption on the active surface sites and to determine the onset of the desorption of oxygen. These studies provided information about the reaction kinetics and the lifetime of the catalyst, as well as the NO scission onset temperature and abatement rate, thus making possible to predict the conversion and define the optimum reaction conditions for efficient NO removal. Catalytic experiments were performed under different operating conditions and feed compositions, such as under rich operation, in presence of oxygen, and in presence of reducing CO and hydrocarbons. The developed nanostructured catalyst exhibits enhanced activity at lower temperatures in comparison to that reported for other Rh-based catalytic systems, while data about feed composition effects and carbon support depletion provided operating conditions that suppress $N_2O$ formation and extent the catalyst lifetime.



## 1. Introduction

Nitrogen oxides ($NO_x$) are major air pollutants generated from the reaction of nitrogen and oxygen in air during combustion processes, such as in power plants and automotive engines [1,2]. In areas of high motor vehicle traffic, the amount of $NO_x$ emitted into the atmosphere can be quite significant resulting in smog and acid rain and the formation of tropospheric ozone. Despite the fact that NO is unstable thus its self-decomposition should be thermodynamically favored ($2NO \rightarrow N_2 + O_2$, $\Delta G^\circ = -86$ kJ/mol) [3], appropriate catalytic systems are necessary in order to reduce the high activation barrier accompanied with the decomposition reaction (364 kJ/mol) [3,4].

Considerable efforts have been made on the catalytic removal of $NO_x$, with a widely established approach being the selective catalytic reduction (SCR) using a variety of reducing agents, such as CO, hydrogen, ammonia, and hydrocarbons [5]. CO is present in the exhausts of several combustion processes and under certain conditions exhibits a good reducing activity converting NO to $N_2$, while it is oxidized into $CO_2$, thus limiting the amounts of two major air pollutants [6]. The use of hydrocarbons is also considered a valuable option due to safety in handling compared to several other reducing agents such as ammonia, low cost, and availability in the exhaust systems after incomplete combustion [7]. To this extent, various catalytic systems for hydrocarbon-SCR have been investigated using combinations of inorganic porous supports (alumina, zeolites) with noble and non-noble metals and metal oxides, and different hydrocarbon molecules [8,9]. However, in most of the cases, the catalysts suffer from low activities, narrow operation temperature range, and limited robustness, characteristics that compromise their use in the automotive industry [10]. The problem becomes even more challenging when the availability of CO and hydrocarbons in the exhaust is limited (lean-burn engine operation), as the catalysts are then required to efficiently operate at excess-oxygen conditions taking full advantage of the limiting amounts of the reducing agents. Techniques that have been developed for efficient lean-burn engine operation include $NO_x$ storage and reduction (NSR) [10,11] and ammonia-SCR, yet still encountering serious drawbacks, such as low selectivity, thioresistance [12], and safety limitations [13].

Nanoscale catalyst design has a high potential to alleviate problems associated with typical systems due to their unique size-, structure-, and morphology-dependent catalytic performance that can be substantially different than those of their bulk counterparts [14]. To this extent, fine control of shape, size, structure, chemical composition, and surface properties of nanoparticles [15,16], and fundamental understanding of their interaction with the support [17] are critical. Herein, we prepared a nanocatalyst consisting

* Corresponding authors. Tel.: +30 210 6503972; fax: +30 210 6511766.
*E-mail addresses:* everm@chem.demokritos.gr (E.C. Vermisoglou), groman@chem.demokritos.gr (G.E. Romanos).

0304-3894/$ – see front matter © 2011 Elsevier B.V. All rights reserved.
doi:10.1016/j.jhazmat.2011.07.078

of Rh nanoparticles supported on single wall carbon nanotubes (SWNT) and investigated its performance toward $NO_x$ reduction. Rh exhibits certain advantages that classify it among the most effective catalysts for $NO_x$ elimination including high activity toward both NO dissociation and CO oxidation, high selectivity toward $N_2$ formation, high reduction rates compared to Pd or Pt, and good resistance to thermal degradation [18,19]. To this extent, several mechanisms have been proposed [20–23] to exemplify the role of the metal on the various reaction steps, i.e. $NO_x$ adsorption, dissociation, recombination, and desorption, and how activity and selectivity depend upon active crystal facets, binding behavior, on-surface mobility/clustering, and antagonistic species effects. Regarding the selection of the support, carbon nanotubes (CNTs) have shown great promise in heterogeneous catalysis due to their graphitic character, mechanical and chemical robustness, high surface area and functionalization flexibility, and a porous morphology that can efficiently suppress internal mass transfer limitations during catalytic processes [17,24,25]. For $NO_x$ conversion in particular, CNTs could also enhance oxygen desorption, which is the rate limiting step and leads to fast catalyst deactivation by saturation of the surface with adsorbed oxygen, as well as improve $N_2$ selectivity over $N_2O$, which is a greenhouse gas formed upon incomplete reduction of NO particularly under cold start engine temperatures.

The performance of the Rh/SWNTs nanocatalyst is investigated under different operating conditions (temperature, partial pressures) and feed compositions (rich conditions, presence of oxygen, reducing CO and hydrocarbons). Gravimetric analysis was employed for the first time to elucidate the mechanism of NO adsorption on the active surface sites and to determine the onset of the desorption of oxygen. Under certain conditions, enhanced activity at lower temperatures was achieved in comparison to that reported in the literature for $Rh/Al_2O_3$, $Rh/SiO_2$, and Rh/multiwall CNTs (MWNTs) systems, which is particularly advantageous for application under cold start engine conditions. SWNTs, which are used in this work, exhibit a distinct set of properties that differentiate them from MWNTs. Specifically, they exhibit higher BET surface area and a large population of surface functionalities [26] that enable higher particle dispersibility. Other important properties of SWNTs in contrast to MWNTs and other graphitic nanostructures include enhanced conductivity, porosity, and semiconducting or metallic behavior depending on the chirality. These properties are critical when these materials are used as supports in heterogeneous catalysis and can affect catalytic activity [27].

Recent reports have shown that CNTs are resistant against oxidation during $NO_x$ conversion (up to 450 °C in the presence of oxygen) and only contribute as $Rh^0$ particle stabilizers [28,29]. On the other hand, there are studies indicating that CNTs are partially oxidized under shortage of reducing agents [30,31] and that the oxidation has a beneficial effect on the NO abatement efficiency as the carbon support acts as a reducing agent assisting the desorption of oxygen from the metal particles. However, in all these studies there is not discussion concerning the form of carbon material that participates in the NO abatement reaction paths. Indeed, it is known that CNTs cannot be produced with a purity of more than ~80% and that the amorphous carbon content, including surface functional groups, is much more sensitive in oxidising conditions. In this regard, the results reported here on the cooperative action of PEG, amorphous carbon content, SWNTs, and the externally fed reducing agents provide optimized conditions for high activity–high selectivity performance in conjunction to extended catalyst lifetime. Concerning the latter, the catalytic tests were performed with high NO gas hourly space velocity (GHSV) of 140–205 $h^{-1}$ when the usual GHSVs for testing are from 10 to 20 $h^{-1}$ and the catalyst operated very efficiently for more than 30 h on stream.

## 2. Experimental

### 2.1. Materials

The SWNTs used in this work were purchased from Carbon Solutions, Inc. According to the manufacturer, the SWNTs were synthesized by electric arc discharge using Ni/Y catalyst and the distribution of their outer diameters is centered around 1.4 nm with a length distribution between 0.5 and 1.5 μm. In addition, they have undergone post-synthesis acidic purification yielding a carbonaceous purity of ~90%. Their BET surface area, as determined by liquid nitrogen porosimetry, is 210 $m^2/g$, while for comparison, that for MWNTs usually resides in the area of 100 $m^2/g$. PEG 200 was supplied by Fluka Chemie GmbH and rhodium chloride hydrate ($RhCl_3 \cdot H_2O$) was supplied by Alfa Aesar.

### 2.2. Preparation of PEG-functionalized, Rh-decorated SWNTs

In a typical synthesis experiment, 50 mg acid-treated SWNTs containing 1.0–3.0 at.% carboxylic acid groups were dispersed in 20 ml PEG 200 under sonication. 0.01 g rhodium(III) chloride hydrate was added in 10 ml PEG 200. The two solutions were mixed together by stirring under reflux for 1 h. The final solution was washed/centrifuged several times using ethanol in order to remove the excess PEG and obtain a clear supernatant, and the sample was left to dry in air. PEG acts as both surfactant and $Rh^{3+}$ reducing agent [32], assisting the spontaneous deposition and stabilization of the Rh particles on the external surface of the SWNTs.

### 2.3. Characterization

Raman measurements were performed in backscattering configuration using a Renishaw inVia Reflex microscope with a high power near infrared (NIR) diode laser ($\lambda$ = 785 nm, $E$ = 1.58 eV) as excitation source. The laser light was focused on the samples using a long working distance (8 mm) 50× (NA = 0.55) objective of a Leica DMLM microscope at power density lower than 0.05 mW/$\mu m^2$ (~1% of full power) to avoid sample heating, using a scan time of 30 s. A dielectric edge filter for Rayleigh rejection at 785 nm with cutoff at approximately 100 $cm^{-1}$ was used for collection of the spectra. Samples for transmission electron microscopy (TEM) were diluted in ethanol and deposited on Lacey C-coated Cu grids and analyzed using a JEOL 2011 HR-TEM, operating at 200 kV. TGA characterization was performed on a Pyris Diamond TG/DTA, Thermogravimetric/Differential, Thermal Analyser (PerkinElmer Instruments). Samples for X-ray diffraction were deposited in the form of powder on a glass. The instrument used was a Siemens D500 X-ray diffractometer.

### 2.4. Adsorption measurements

The NO, CO gas adsorption measurements were performed with a gravimetric microbalance (MK2-M5, CI Electronics, LTD). The masses of the sample and counterweight pans, the hooks, the counterweight material and the hang chains of the microbalance assembly were of the order of 1–300 mg per item and were defined with an accuracy of ±0.1%. The materials were appropriately selected to induce a symmetrical configuration to the balance setup in order to minimize buoyancy effects. The microbalance had a 0.1 μg stable resolution. The densities of the bulk gas phase that were applied for the buoyancy correction of both the transient and equilibrium data were calculated using the Benedict–Webb–Rubin equation of state for CO and NO. The referred uncertainty for this equation lies in the order of 3% [33].

### 2.5. Catalytic performance experiments

Catalytic activity data were obtained using a conventional fixed-bed flow reactor at atmospheric pressure as described in our previous work [34]. A quartz tube with an inner diameter of 2.8 mm was chosen as the reactor tube. A mass of 100 mg of the catalyst was placed at the middle part of the tube and packed within two pieces of glass wool. The temperature was controlled within a maximum variation of 0.2 °C by a PID automatic temperature controller. The gas stream was preheated at the same temperature before entering the reactor bed. The gas leaving the reactor was analyzed at 30 min intervals by a Gas Chromatograph equipped with a 6-port gas sampling valve and thermal conductivity (TCD)-flame ionization (FID) detectors in series. A 30 feet packed column (HeysepD) allowed for the separation of the gases of interest (NO, $N_2O$, $N_2$, CO, $CO_2$, $O_2$, $C_3H_6$) within 20 min and 10 more minutes were necessary to allow for the cooling of the chromatograph oven to be ready for the subsequent chromatographic run. In this study, catalytic activity using simulated exhaust gases was mainly measured as a function of temperature and CO/NO ratio, in rich conditions and as a function of $C_3H_6$ concentration in the presence of $O_2$ at an elevated temperature of 523 K. Water vapor was not introduced in the gas streams in order to avoid complex effects of water gas shift reaction (CO) and hydrocarbon reforming. A typical feed composition of simulated exhaust gas was 3.5%$_{vol}$ CO, 18%$_{vol}$ $C_3H_6$, 3.5%$_{vol}$ NO, 39%$_{vol}$ $CO_2$, and the balance He. The temperature range examined at this composition was from 423 to 523 K. In another composition the $O_2$ concentration at 523 K was kept at 10 %$_{vol}$ and $C_3H_6$ concentration changed 3 times between 13%$_{vol}$ and 2.5%$_{vol}$ from rich to stoichiometric conditions. Space velocity was kept at 5500 $h^{-1}$.

## 3. Results and discussion

The stoichiometry number, *St*, used to identify the redox characteristic of the model gas mixtures is defined as in formula (1).

$$St = \frac{2[O_2] + [NO]}{[CO] + 9[C_3H_6]} \quad (1)$$

When $St < 1$, $St = 1$, and $St > 1$, the composition of the feed stream is net reducing, stoichiometric, and net oxidizing, respectively. Discussions on the performance of the catalyst in reducing conditions were based on the conversion of NO ($R$), the selectivity for $N_2$ ($S$) and the fraction of the oxygen desorbed either through the oxidation of CO ($Y_{CO}$) or through the depletion of the catalyst support ($Y_{SUP}$). The following equations were used to derive the aforementioned factors:

$$R = \frac{\%_{vol}NO_{feed} - \%_{vol}NO_{outlet}}{\%_{vol}NO_{feed}}, \quad S = 2\frac{\%_{vol}N_{2outlet}}{\%_{vol}NO_{feed} - \%_{vol}NO_{outlet}}$$
$$Y_{CO} = \frac{\%_{vol}CO_{feed} - \%_{vol}CO_{outlet}}{\%_{vol}NO_{feed} - \%_{vol}NO_{outlet}}, \quad Y_{SUP} = \frac{\%_{vol}CO_{2outlet} - \%_{vol}CO_{2feed}}{\%_{vol}NO_{feed} - \%_{vol}NO_{outlet}} - Y_{CO} \quad (2)$$

### 3.1. Structural and morphological evaluation of the Rh/SWNTs

The Raman spectrum of the Rh-decorated SWNTs in comparison to as-received SWNTs is illustrated in Fig. 1(a). The high graphitic quality of the nanotubes is confirmed by the strong radial breathing mode (RBM) peak at 163 $cm^{-1}$, and by the high intensity ratio of the G over D band, which expresses the highly graphitized carbon in relation to lattice disorders or amorphous carbon contributions. In addition, the high crystalline quality of the nanotubes is indicated by the fact that the G′-band exhibits a strong signal and is completely free from defect contributions [35]. Comparing the Rh/SWNT spectrum with that of the pristine SWNT, we observe a significant enhancement of the RBM peak intensity after Rh decoration by a factor of ~3.5, which has also been observed in our previous work on Au/SWNT composites [34], as well as enhancement of the $I_G/I_D$ intensity ratio and of the intensity of the G′ line. This Raman enhancement is attributed to the induced electric field of the metallic nanoparticles acting on the SWNTs, as well as to the existence of enhanced electromagnetic fields inside cavities formed between nanoparticles with a separation of the order of a few nanometers, in the proximity of the SWNTs [36,37].

XRD analysis (Fig. 1(b)) depicts the characteristic peaks of metallic Rh at 2$\theta$ of 41.05°, 47.64°, and 69.8°, corresponding to diffraction from the (1 1 1), (2 0 0), and (2 2 0) crystallographic planes, respectively. The (1 1 1) facet in particular, has been shown to be especially active for the promotion of NO decomposition [20]. Applying the Scherrer formula, which correlates the size of crystallites to the broadening of the main diffraction peak, a value of 17 nm was extracted for the mean size of the ordered domains. Rh crystallites and SWNTs are organized into larger assemblies having an average size of 40 nm, as shown in the TEM image in Fig. 1(c). The dark field and higher resolution TEM images in Fig. 1(d) and (e), respectively, reveal an average crystallite size of about 10–15 nm, which is in good agreement to the value extracted from the Scherrer method. The existence of SWNTs is confirmed by the high resolution TEM image of Fig. 1(f) showing a close view of a bundle consisting of SWNTs. The XRD peaks at 44.41°, 51.83°, and 76.39° correspond to (1 1 1), (2 0 0), (2 2 0) planes of FCC Ni indicating that despite the fact that the nanotubes have undergone post-synthesis processing for the removal of the metal catalysts used for growth, they still contain an amount of remnant Ni particle impurities. Despite the fact that a contribution to the activity of the catalyst by these particles is inevitable, this is expected to be relatively minor compared to the Rh effect, based on comparative studies demonstrating low activity of carbon-supported Ni toward $NO_x$ reduction, especially at temperatures lower than 473 K [38].

Fig. 2 shows the TGA profile of the Rh-doped SWNTs in comparison to pristine SWNT and pure PEG 200 in a temperature range of 30–1200 °C (up to 400 °C for PEG 200) under oxygen flow. Oxidation of PEG takes place in a single step of almost total weight loss occurring between 110 and 240 °C. In the pristine SWNTs sample, the first steep weight loss up to about 150 °C corresponds to the amount of water that desorbs from the hydrophilic surface of the nanotubes, which have been functionalized by –COOH groups during the acid purification step. Oxidation of amorphous carbon impurities from the pristine SWNT sample starts at 230 °C and proceeds through a drop of weight up to 460 °C. This transition includes the removal of the –COOH functional groups, yet, at this stage, further oxygenation of the nanotubes surface may also occur upon TGA. A steep weight drop follows up to 510 °C, which corresponds to oxidation of SWNTs, with a maximum mass loss rate observed at 498 °C. A second major yet smoother step appears in the range of 520–780 °C reflecting gradual oxidative decomposition of SWNTs bundles until complete combustion. The fact that SWNT combustion does not take place in one single step is also attributed to the post-synthesis acidic processing that creates defects to the nanotubes. The slight slope change at about 650 °C indicates that graphitic particles that are included in the pristine sample as impurities start oxidizing at this temperature. Upon completion of carbon decomposition, a residual weight of 6.7% was found, which is attributed to the residual Ni catalyst particles that upon TGA have been transformed to nickel oxide (NiO). Based on that, the content of Ni particles is calculated to be 5.2%.

Concerning the TGA curve of Rh-doped SWNTs, all characteristic steps observed in the pristine SWNT sample (amorphous carbon combustion, steep and smoother SWNT oxidation) are also present here, but all take place at lower temperatures. In addition, PEG removal is expected at relatively low temperatures, based on the TGA profile of the pure PEG shown in Fig. 2. The maximum decomposition rate for the graphitic part of the Rh-doped SWNTs was at 390 °C, in contrast to 498 °C for the pristine SWNT sample. Moreover, the smoother weight loss step at high T resembling to the

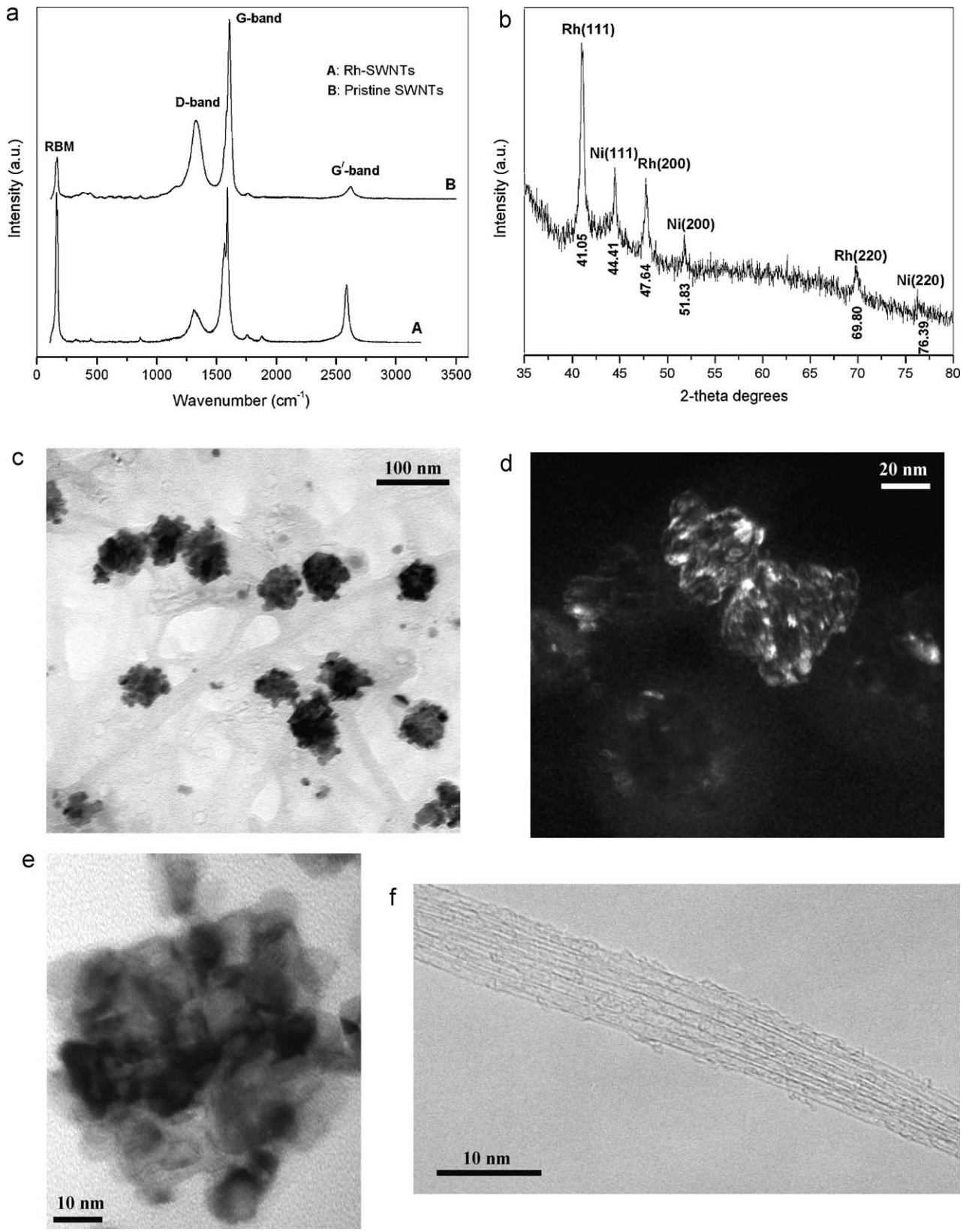


**Fig. 1.** (a) Raman spectra of pristine and Rh-decorated SWNTs. (b) XRD pattern of the Rh-decorated SWNTs. (c) Particle dispersion in the Rh/SWNT composite. (d) Dark-field TEM revealing the Rh crystallites. High resolution TEM images of (e) a particle assembly and (f) a nanotube bundle indicating the existence of SWNTs.

corresponding gradual step of the pristine SWNTs was found to begin at 460 °C versus 520 °C for the pristine sample. Complete decomposition of the Rh-doped SWNTs occurred also at lower temperature (670 °C), at which the remained mass corresponds to a 9.7%. For comparison, the combustion of the pristine SWNTs at the same temperature was still in progress with a remaining mass of 18.5%. The lowering in oxidation temperature of SWNTs upon Rh decoration suggests that the oxidation of CNTs is catalyzed by the

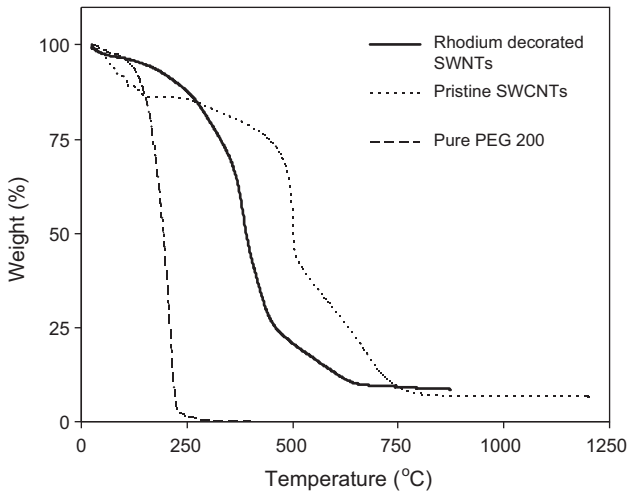


**Fig. 2.** TGA of Rh-doped SWNTs versus pristine SWNTs and pure PEG 200.

Rh nanoparticles. A similar effect has been reported upon thermal oxidation of CNTs doped with La particles, where La acts as an oxygen reservoir by forming LaO and $O_2$ molecules dissociate on the LaO surface to atomic oxygen that probably migrates and reacts with carbon upon heating under $O_2$/air [39]. The Rh loading estimated by the TGA curves of the Rh-doped and pristine SWNTs after correcting for oxide formation is about 2% w/w.

### 3.2. Adsorption experiments

#### 3.2.1. Adsorption of NO and CO at different temperatures

Adsorption results provided information on the onset temperature for the catalytic scission of NO by the developed Rh/SWNTs catalyst and served the purpose of defining the optimum reaction conditions for the efficient abatement of $NO_x$ from a gaseous stream, by means of a packed bed microreactor. Moreover, by interpreting the transient results of adsorption it was possible to end up with conclusions about the reaction kinetics and the lifetime of the catalyst, which is limited by the stoichiometric oxidation of the support material.

In the recent literature dealing with the application of carbon materials as supports for the development of NO depleting catalysts [29–31] the following reaction steps have been proposed:

$$NO_{(g)} + * \Leftrightarrow * - NO \quad (3)$$

$$* - NO + * \rightarrow * - N + * - O \quad (4)$$

$$2 * - N \rightarrow N_{2(g)} + 2* \quad (5)$$

$$2 * - O + C \rightarrow CO_{2(g)} + 2* \quad (6)$$

$$* - O + C \rightarrow CO_{(g)} + * \quad (7)$$

where the first two equations describe the adsorption and dissociation of NO on the active metal centers of the catalyst which are denoted with an asterisk, and Eqs. (5)–(7) demonstrate the desorption pathways for nitrogen and oxygen in the form of $N_2$, CO and $CO_2$. It is already defined that significant desorption of $O_2$ from Rh (1 1 1) surfaces occurs only at temperatures above 1000 K [40], a fact that designates oxygen desorption as the rate determining step of the overall reaction mechanism. Thereby, at temperatures up to 523 K, as those applied in this work, the experimentally confirmed oxygen desorption (loss of mass) proceeded exclusively via the stoichiometric oxidation of the support material and the formation of CO and $CO_2$. The overall reaction can be regarded as a catalytic reduction of NO with carbon as the reducing agent and is

**Table 1**
Adsorption experiments conditions and mass loss data.

| | Sample mass (mg) | Period of experiment (h) | Mass loss (%) |
|---|---|---|---|
| Initial outgassing at 453 K | 28.23 | 24 | N/A |
| NO adsorption at 323 K | 28.88 | 42 | −2.3 |
| Outgassing at 453 K | | 24 | |
| NO adsorption at 383 K | 28.23 | 20 | 0 |
| Outgassing at 453 K | | 24 | |
| NO adsorption at 400 K | 27.98 | 68 | 0.9 |
| Outgassing at 453 K | | 24 | |
| NO adsorption at 423 K | 27.65 | 21 | 1.2 |
| Outgassing at 453 K | | 24 | |
| NO adsorption at 453 K | 25.81 | 23 | 6.7 |
| Outgassing at 453 K | | 24 | |

expressed with the following equation:

$$2xNO_{(g)} + (y+z)C_{(s)} \rightarrow xN_{2(g)} + yCO_{2(g)} + zCO_{(g)} \quad \text{with} \quad x = E + 0.5z \quad (8)$$

From the results presented in Fig. 3(a), it can be concluded that the exposure of the developed Rh/SWNTs sample at sequentially increasing partial pressures of NO and temperatures above 400 K led to considerable mass reduction due to the abruption of a fraction of the carbon support in the form of CO and $CO_2$. Moreover, as it can be observed in Fig. 3(b), at high surface loadings (300–400 mbar), carbon depletion was initiated even from the moderate temperature of 383 K (Fig. 3(b)). Comparison between the uptake capacity for NO and CO at 323 K (Fig. 3(b)) confirms that the adsorption of NO on the rhodium surface is thermodynamically favored over the adsorption of CO and that the dissociation step (Eq. (4)) can take place at temperatures as low as 323 K and at low NO surface coverage. The intense hysteresis between the adsorption and desorption curve of the NO isotherm at 323 K is another indication of the rhodium-catalyzed scission of NO. Elevated temperatures between 460 and 700 K (the exact value depending on the NO coverage), are usually necessary for desorbing the nitrogen (Eq. (5)) from Rh surfaces that have provoked NO scission. Indeed, most of the NO amount that was adsorbed at 323 K was still retained under high vacuum conditions (Fig. 3(b)) in the form of *–N and *–O, revealing that the forces that keep NO on the catalyst surface were stronger than the van der Waals forces, which characterize physisorption. Indeed, it has been shown that most molecules adsorb weakly and reversibly on the CNT walls with a relatively small charge transfer [41,42]. These molecules can act either as charge acceptors, such as $NO_x$ and $O_2$, or donors, such as $NH_3$ and $H_2O$. In this regard, we can quantify the contribution of the SWNTs in the overall gas uptake by measuring the NO amount that is desorbed during outgassing at high vacuum and 323 K (about 1150 μmol per gram of the overall catalyst, Fig. 3(b)). The amount remaining adsorbed after outgassing is attributed to adsorption by the Rh particles through NO scission and was found to be 1900 μmol per gram of the overall catalyst or else 5.7% of the total catalyst mass. After outgassing at high vacuum and 453 K for 24 h, the NO amount remaining attached on the catalyst surface corresponded to about 2.3% of the total mass of the catalyst (Table 1).

Interesting to note is that the CO uptake on the surface of the Rh/SWNTs catalyst was quite significant. As a comparison, pristine SWNTs (Carbon Solutions Inc.) [43] exhibit less CO adsorption capacity than the Rh decorated ones. The enhanced adsorption of CO on Au and Rh nanoparticle-decorated SWNTs has been recently investigated by means of both theoretical [44] and experimental [45] studies and is attributed to the transfer of electron density from the SWNT to the nanoparticle species during growth and the accompanied transfer of electronic density back into the SWNT dur-

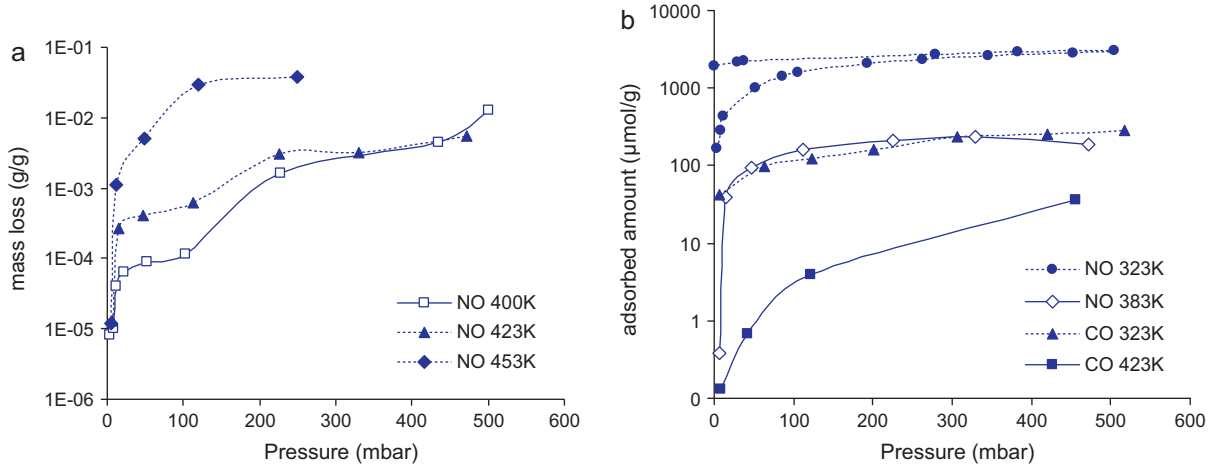


**Fig. 3.** (a) Catalyst mass loss as a function of NO pressure at elevated temperatures. (b) Adsorption of NO at moderate temperatures in comparison with CO adsorption.

ing the adsorption of CO molecules on the nanoparticle surface. This behavior may be very favorable for the catalytic abatement of NO in gaseous streams that contain CO as reducing agent. Although CO may occupy a fraction of the metal surface, the closeness of the CO molecules to the oxygen occupied metal centers *–O will certainly conclude to faster oxygen desorption rate in the form of $CO_2$.

Table 1 gives an overview of the adsorption experiments performed, the sequence by which they were conducted, the total period of the catalyst exposure at NO partial pressures from 10 to 400 mbar, and the total mass loss during these experiments. A first outcome is that carbon depletion starts to be significant at temperatures well above 423 K. At the final temperature of 453 K, the mass loss after 24 h on stream was about 6.7% of the total mass of the catalyst. Overall, after 5 days of experimentation at temperatures above 400 K and NO atmosphere, the total mass loss of the support was 8.6%. The depletion of the support had a negative effect on the effectiveness of the catalyst to dissociatively adsorb the NO as indicated in Fig. 4, where the adsorption curves of the catalyst at 323 K, before and after the experiments at elevated temperatures, are illustrated in comparison. This effect can be attributed to the agglomeration of a fraction of the Rh nanoparticles that have started to lose their firm attachment to the catalyst support. Especially, the reduction

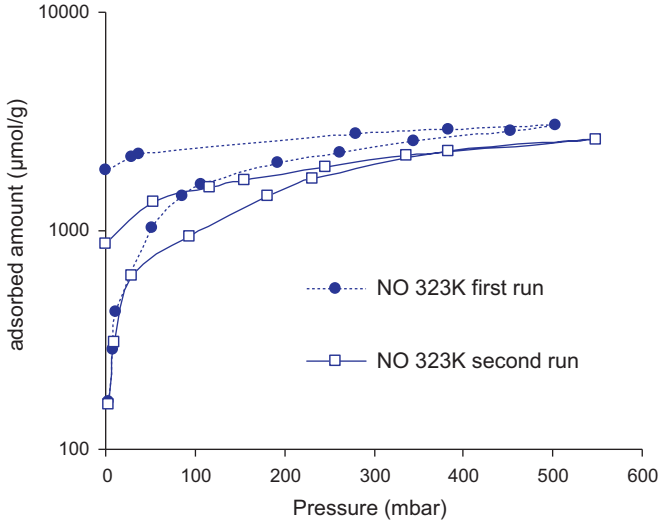


**Fig. 4.** Comparison of NO adsorption capacity of the catalyst at 323 K before and after the experiments at elevated temperatures.

of the dissociation capacity is evident solely in the region of high surface loadings (pressures above 30 mbar) where agglomerated nanoparticles, due to the lower exposed surface area, are incapable to accommodate the same number of adsorbed NO (see Eq. (3)) as before. As can be defined from the adsorption isotherms in Fig. 4, a mass loss of about 9% corresponds to a decrease of the NO scission capacity of about 10%. It should be however noted that the catalyst underwent adsorption tests under very intense oxidizing conditions and that in gaseous streams containing also reducing agents like CO and hydrocarbons the life cycle of the Rh/SWNTs catalyst must be significantly extended.

### 3.2.2. *Interpretation of the transient adsorption curves*

From the transient NO exposure curves, presented in Fig. 5, it can be concluded that the surface loading for the initiation of substrate depletion depends inversely on the temperature. Specifically, the mass loss of the catalyst started to be detectable at NO pressures of 5, 23, 50 and 225 mbar at the experimental temperatures of 453, 423, 400 and 383 K, respectively. Interesting to note is that whenever carbon removal began at low surface coverage (below 100 mbar), like in the case of 423 and 453 K (Fig. 5(c) and (d)), the pressure step was accompanied by an immediate mass uptake followed by an almost linear with time mass decline. In this case the mass uptake corresponds to the adsorption of more NO molecules onto unoccupied active sites of the metallic surface. As soon as NO binds on all available active sites, the catalyst mass decreases continuously from the beginning of a pressure step. By examining the transient curves at elevated temperatures as well as the NO adsorption isotherm at 323 K (Fig. 4), it was concluded that at NO pressure around 100 mbar the surface coverage of the Rh/SWNTs catalyst was complete. The NO loading capacity of the catalyst was 1.62 mmol/g (Fig. 3), and by taking into account the nanoparticle mass percentage (2%, w/w), as derived from the TGA analysis, this is translated to 80 mmol per gram of deposited Rh.

The linear part of the transient curves was further exploited in order to derive the NO abatement rates. Taking into account that the ratio ($k$) of the moles of NO that are reduced over the moles of the carbon removed from the support of the catalyst takes values between 1 and 2 (Eq. (8)), it is possible to express the slopes of the transient curves (mg C/s, Fig. 5) at the steady state conversion in terms of μmol of reduced NO per minute and gram of catalyst. The results for $k = 1.5$ are presented in Table 2. It can be seen that small increments of the temperature from 400 to 423 K and from 423 to 453 K had a significant effect on the NO abatement rate, which became 10–30 times faster. Moreover, the minor effect of the carbon removal on the activity of the catalyst is demonstrated

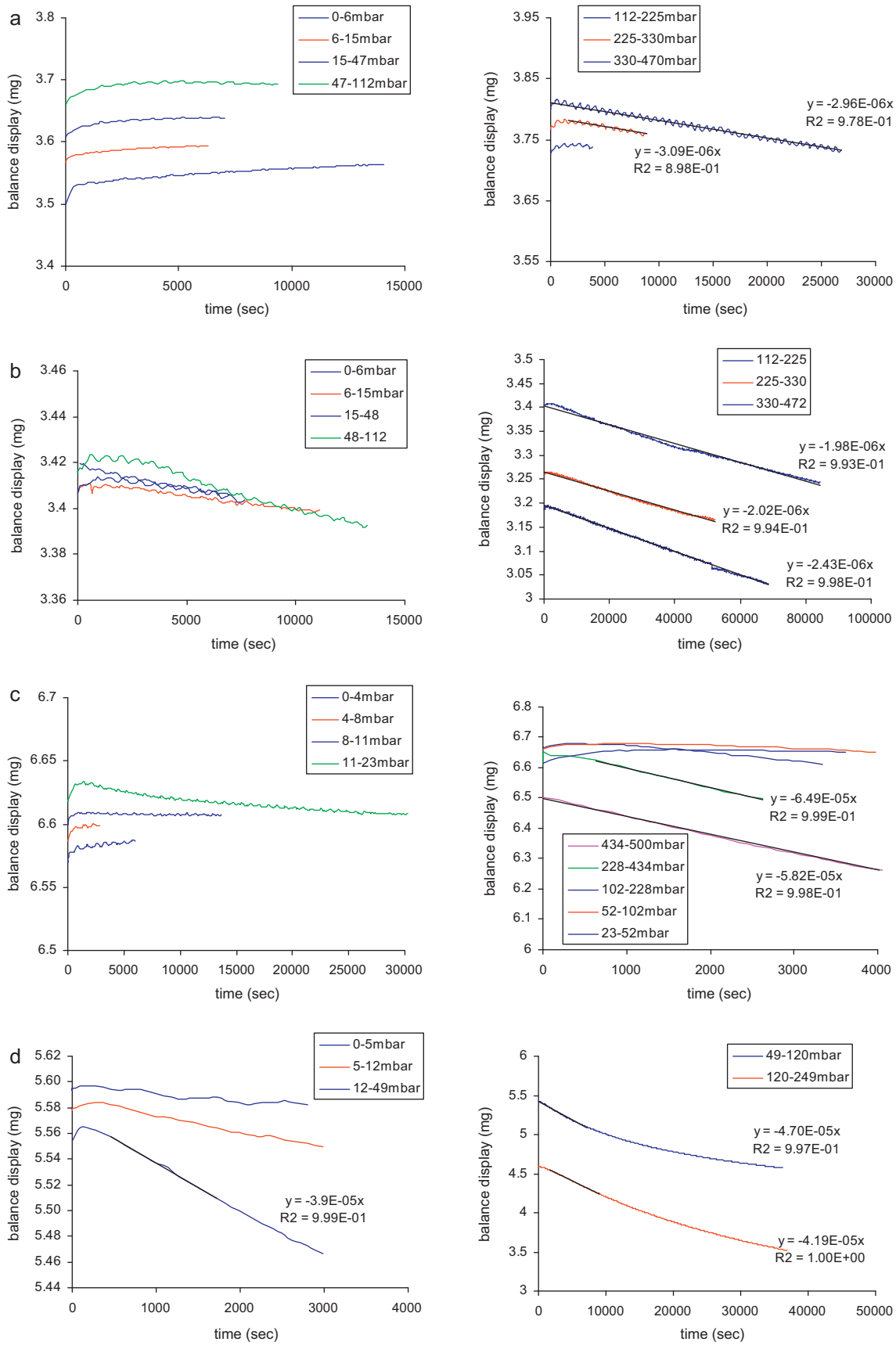


**Fig. 5.** Transient curves of Rh/SWNTs exposure to different NO pressures at (a) 383 K, (b) 400 K, (c) 423 K, and (d) 453 K.

**Table 2**
NO abatement rates derived from the adsorption transient curves.

| $T$ (K) | Pressure (mbar) | | | | | | | |
|---|---|---|---|---|---|---|---|---|
| 383 | **6** | **15** | | **47** | **112** | **225** | **330** | **470** | |
| | *nr* | *nr* | | *nr* | *nr* | *0.52* | *0.828* | *0.793* | (μmol/min/g) |
| 400 | **6** | **15** | | **48** | **112** | **225** | **330** | **470** | |
| | *nr* | *nr* | | *nr* | *0.74* | *0.53* | *0.54* | *0.65* | (μmol/min/g) |
| 423 | **4** | **8** | **23** | | | **230** | **430** | **500** | |
| | *nr* | *nr* | *0.44* | | | *6.9* | *17.63* | *15.8* | (μmol/min/g) |
| 453 | **5** | **12** | | **50** | **120** | **250** | | | |
| | *1.67* | *3.7* | | *11.3* | *13.7* | *12.2* | | | (μmol/min/g) |

*nr* = no reaction observed.

by the small decrease of the reaction rate (about 10%) upon the pressure increments from 430 to 500 mbar at 423 K and from 120 to 250 mbar at 453 K.

The higher importance of the above experiments was that they provided a rough approximation of the NO abatement rate, thus making possible to predict the conversion that will be achieved in a packed bed microreactor under certain conditions. As a case study, Fig. 6 illustrates the catalytic conversion obtained by 100 mg of the Rh/SWNTs material at 453 K under the conditions described in Table 3. Helium was used as the balance gas of the mixture. Introducing the data of the table in the following equations, it was possible to calculate the total time ($t$) of NO residence in the reactor in contact with the catalyst, the amount ($A$) of NO reduced during this period, and from these, the $R$% NO conversion:

$$t = \frac{L \times S}{F \times \%_{vol}NO_{feed}}, \quad A\,(ml) = K \times t \times m \times 0.0224,$$

$$R = \frac{A}{F \times t \times \%_{vol}NO_{feed}} \tag{9}$$

A conversion value of 0.021 was predicted under these conditions, which comes into convergence with the experimentally obtained conversion in the steady state conditions achieved after about 120 min on stream (see Fig. 6).

### 3.3. Catalytic conversion

#### 3.3.1. Rich conditions at different temperatures and CO/NO ratios

The examination of the effect of temperature and CO/NO ratio on the NO abatement efficiency of the catalyst, at rich conditions, was performed at a stoichiometry number *St* of about 0.02. Five catalytic tests were conducted and Table 4 pertains to the complete set of experiments and the corresponding figures, together with the definition of the flow/bed parameters, feed composition, regeneration procedure, and the steady state performances and concentrations in the outlet of the reactor. The calculation concerning the $N_2$, $N_2O$ selectivity and the fraction of oxygen desorbed either through CO oxidation or substrate depletion was performed according to the

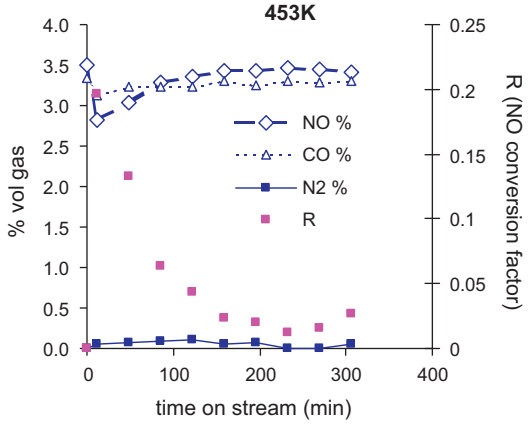


**Fig. 6.** Gas phase concentration and NO conversion evolution in a fixed-bed flow reactor accommodating 100 mg of the catalyst.

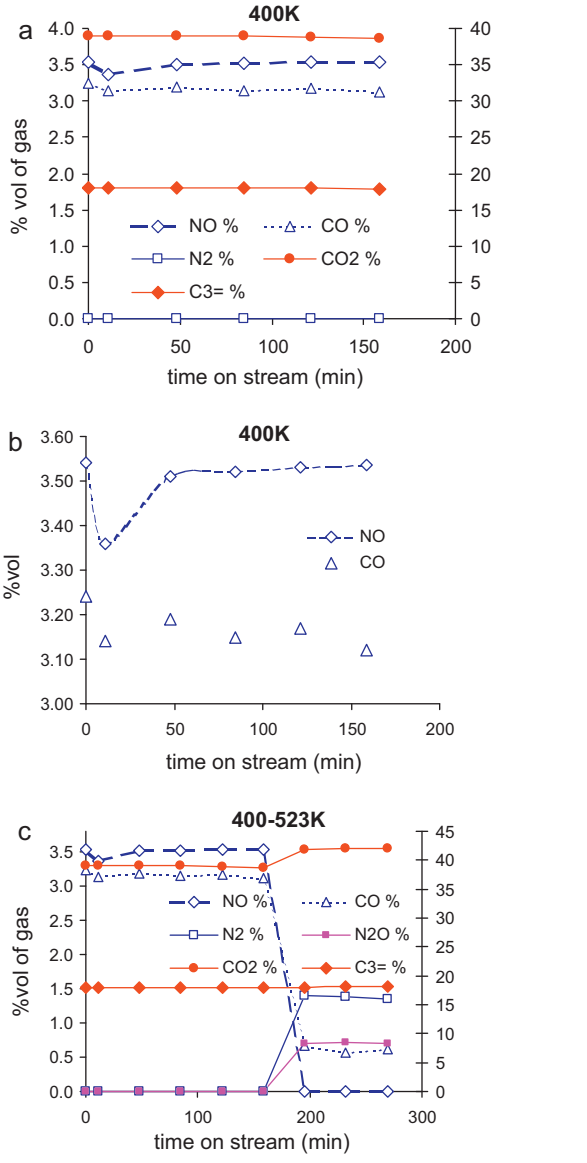


**Fig. 7.** Reactor outlet concentration (a) at 400 K – red symbols correspond to the secondary $y$-axis, (b) at 400 K – detail for NO and CO. (c) Effect of temperature increase to 523 K. (For interpretation of the references to color in this figure legend, the reader is referred to the web version of the article.)

**Table 3**
Conditions for NO conversion in a fixed-bed flow reactor at 453 K.

| Catalyst mass (m) (g) | Bed volume (ml) | Bed length (*L*) (cm) | Bed cross-section (*S*) ($cm^2$) | *T* (K) | Reaction rate (*K*) (μmol/min/g) | Total flow rate (*F*) (ml $min^{-1}$) | $\%_{vol}$ gas feed | | | |
|---|---|---|---|---|---|---|---|---|---|---|
| | | | | | | | NO | CO | $C_3$ | $CO_2$ |
| 0.1 | 0.47 | 7.7 | 0.0615 | 453 | 11.3 | 43 | 3.1 | 3.6 | 17.8 | 29.2 |

stoichiometry of the reaction $2NO + 2CO \leftrightarrow N_2 + 2CO_2$ by using Eq. (2).

As observed in Fig. 7(a), during the initial stages (10 min) of the first catalytic test that took place at the lower temperature (400 K) there was a small decrease of the NO and CO concentration in the outlet stream, which however, was not accompanied with the appearance of $N_2$ or the increase of the $CO_2$ concentration. The relative pressure of NO in the feed was 36 mbar and as already concluded from the adsorption results (Table 2), for small NO pressures up to 48 mbar and at the temperature of 400 K the surface coverage of the Rh catalyst is not so extended for $N_2$ desorption and substrate depletion to occur. Thereby, the disturbance of the NO and CO concentration in the outlet of the reactor can be regarded as the result of adsorption. An interesting remark coming out from Fig. 7(b) is that the mechanism of adsorption-dissociation of NO on the Rh catalyst is much faster than the mechanism of CO adsorption, which continued to evolve even after 3 h on stream.

The effect of dynamically increasing the temperature up to 523 K is illustrated in Fig. 7(c). The NO conversion factor *R* was 1 and remained stable for more than 2 h on stream, whereas the selectivity *S* for $N_2$ during this period has been slightly altered from 0.79 down to 0.76. Indeed, although $3.54\%_{vol}$ of NO was fully abated on the catalyst, the $N_2$ concentration in the exhaust was about $1.4\%_{vol}$, instead of $1.77\%_{vol}$, as would be expected for an $N_2$ selectivity value of $S = 1$. Moreover, although the feed concentration of CO ($3.24\%_{vol}$) was below the stoichiometric ratio for the reaction $2NO + 2CO \leftrightarrow N_2 + 2CO_2$, there was a considerable amount of CO remaining in the exhaust stream ($\sim 0.62\%_{vol}$) that is attributed to the contribution of the support as a reducing agent. Indeed, a fraction of the adsorbed oxygen was removed through the oxidation of CO, $Y_{CO} = 0.74$, another fraction through the support depletion, $Y_{SUP} = 0.135$, and the rest 0.125 as $N_2O$. In this context, we can claim that the presence of the reducing gas can considerably enhance the lifetime of the catalyst especially when working at temperatures above 500 K. The $CO_2$ concentration has been increased by a percentage of $3.1\%_{vol}$ instead of $3.54\%_{vol}$ as would be expected from the complete abatement of NO, a fact that further evidences the desorption of part of the adsorbed oxygen as $N_2O$.

During the second catalytic test (Fig. 8(a)) performed at 473 K with a stoichiometry number *St* of 0.0195, the NO conversion factor achieved at the first 10 min on stream was $R = 1$ (regarded as both adsorption and conversion) and reached a steady state value of 0.42 within the next 2 h. This efficiency is significantly higher than those referred in the recent literature for catalytic systems of Rh-decorated MWNTs [30,31] and Rh decorated silica [2,46] and alumina supports [2,47,48], and is attributed to the use of SWNTs support, to the good dispersion, small size, and firm contact of the Rh crystallites with our SWNTs facilitated by PEG functionalization, and to the beneficial contribution of the carbon matrix which acts as a reducing agent that facilitates oxygen desorption at lower temperatures. The $N_2$ selectivity was 0.96 compared to the 0.76 obtained for almost the same *St* value (1st catalytic test), at higher temperature (523 K) and at CO/NO ratio <1, a fact indicating the beneficial effect of the excess CO on the preferable desorption of oxygen as $CO_2$ rather as $N_2O$. Rising the temperature up to 523 K led again to NO conversion factor of $R = 1$ but in this case, due to the excess CO, the selectivity for $N_2$ was $S = 1$. Moreover there was a slight indication of substrate depletion. The positive effect of CO is also evidenced in the third experiment (Fig. 8(b)), which was performed at 473 K and a stoichiometry number *St* of 0.0144, but in a high excess of CO (CO/NO = 1.44). The NO conversion factor in this case was $R = 1$ during 4.5 h on stream, the $N_2$ selectivity was $S = 1$, and there was no indication for depletion of the support.

The beneficial contribution of the support on the efficiency of the Rh catalyst was proclaimed during the 4th experiment. Working at a CO/NO ratio of 0.95 and at very low temperature (423 K) we

**Table 4**
NO abatement catalytic experiments under rich conditions at different temperatures and CO/NO ratios.

| | | | | | | |
|---|---|---|---|---|---|---|
| **1st test**. Fig. 7(a)–(c). Regeneration conditions: 6 h 350 °C with helium and overnight 200 °C with helium. St/GHSV/total flow-0.0215/5473 $h^{-1}$/43 ml $min^{-1}$ | | | | | | |
| | **NO** | **$N_2$** | **$N_2O$** | **CO** | **$CO_2$** | **$C_3H_6$** |
| **Feed concentration** | 3.54 | 0 | 0 | 3.24 | 39.0 | 17.99 |
| | ***R*** | ***S*** | ***S*** | $Y_{CO}$ | $Y_{SUP}$ | $Y_{N2O}$ |
| 400 K | – | – | | – | – | – |
| 523 K | 1 | 0.76 | 0.2 | 0.74 | 0.135 | 0.125 |
| **2nd test**. Fig. 8(a). Regeneration conditions: 5 h 350 °C with helium and overnight 200 °C with helium. St/GHSV/total flow-0.0195/5473 $h^{-1}$/43 ml $min^{-1}$ | | | | | | |
| **Feed concentration** | 3.14 | 0 | 0 | 3.22 | 32.45 | 17.55 |
| | ***R*** | ***S*** | ***S*** | $Y_{CO}$ | $Y_{SUP}$ | $Y_{N2O}$ |
| 473 K | 0.42 | 0.96 | | 1.06 | 0 | – |
| 523 K | 1 | 1 | 0.0 | 0.99 | 0.074 | – |
| **3rd test**. Fig. 8(b). Regeneration conditions: 6 h 350 °C with helium and overnight 200 °C with helium. St/GHSV/total flow-0.0144/5473 $h^{-1}$/43 ml $min^{-1}$ | | | | | | |
| **Feed concentration** | 2.44 | 0 | 0 | 3.52 | 30.3 | 18.46 |
| | ***R*** | ***S*** | ***S*** | $Y_{CO}$ | $Y_{SUP}$ | $Y_{N2O}$ |
| 473 K | 1 | 1 | 0 | 1 | 0 | – |
| **4th test**. Fig. 8(c). Regeneration conditions: 6 h 350 °C with helium and overnight 150 °C with helium. St/GHSV/total flow-0.0218/5473 $h^{-1}$/43 ml $min^{-1}$ | | | | | | |
| **Feed concentration** | 3.502 | 0 | 0 | 3.334 | 36.6 | 17.508 |
| | ***R*** | ***S*** | ***S*** | $Y_{CO}$ | $Y_{SUP}$ | $Y_{N2O}$ |
| 423 K | 0.03 | 1 | 0 | 0.74 | 0.27 | – |
| **5th test**. Fig. 8(d). Regeneration conditions: 6 h 350 °C with helium and overnight 180 °C with helium. St/GHSV/total flow-0.0190/5473 $h^{-1}$/43 ml $min^{-1}$ | | | | | | |
| **Feed concentration** | 3.11 | 0 | 0 | 3.58 | 29.2 | 17.79 |
| | ***R*** | ***S*** | ***S*** | $Y_{CO}$ | $Y_{SUP}$ | $Y_{N2O}$ |
| 453 K | 0.1 | 0.96 | 0 | 0.81 | 0.24 | – |

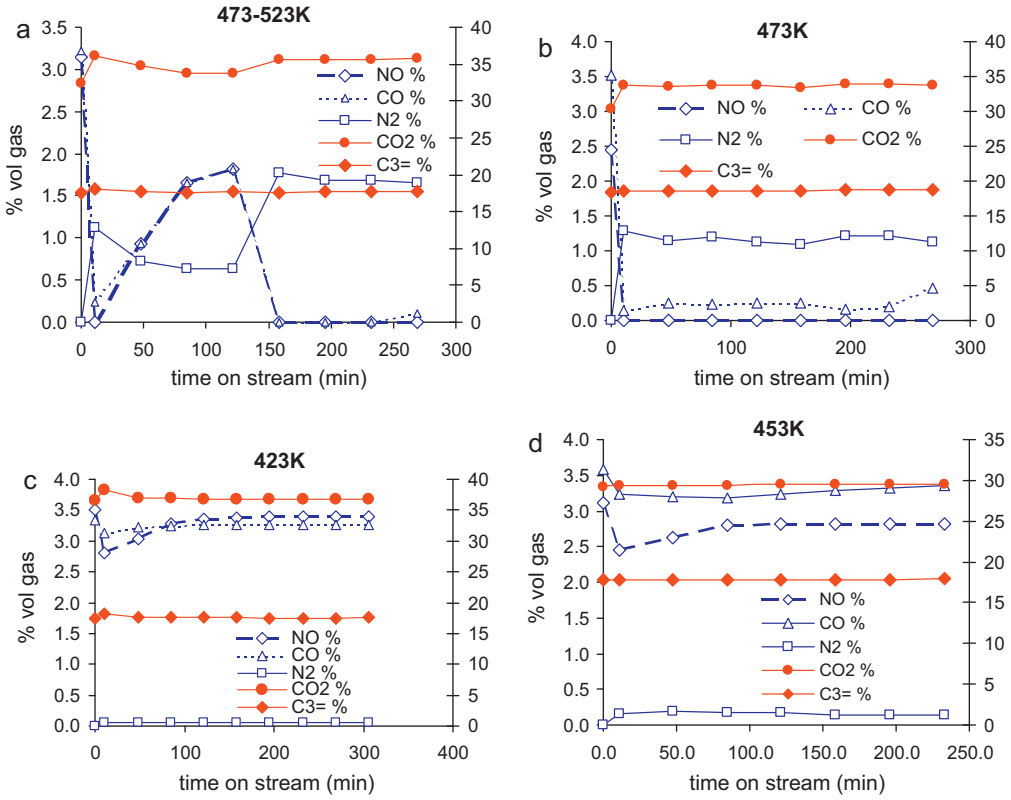


**Fig. 8.** Reactor outlet concentration (a) at 473–523 K and CO/NO = 1.024, (b) at 473 K and CO/NO = 1.44, (c) at 423 K and CO/NO = 0.95, (d) at 453 K and CO/NO = 1.15. Filled symbols correspond to the secondary *y*-axis.

obtained a steady state NO conversion of $R = 0.03$ with $N_2$ selectivity $S = 1$. The fraction of oxygen desorbed as CO was $Y_{CO} = 0.74$ and the fraction desorbed through the support depletion was $Y_{SUP} = 0.27$. It should be noted that this is the first time that NO abatement even of the order of 3% is reported at such a low temperature. At a CO/NO ratio of 1.15 and 453 K (5th experiment) the steady state conversion was more prominent reaching the value of $R = 0.1$ with $N_2$ selectivity $S = 0.96$ and oxygen desorption fractions of $Y_{CO} = 0.81$ and $Y_{SUP} = 0.24$.

From the results presented in this section it can be concluded that the contribution of the support in the oxygen desorption from the catalyst surface starts to be significant at moderate temperatures below 473 K and depends on the CO/NO ratio; e.g. lower ratio results to higher fraction of oxygen desorbed through support depletion. At the highest examined temperature of 523 K the support contribution was significant only for a moderate CO/NO ratio of 0.9. This was also the only test where desorption of oxygen as $N_2O$ was observed. The catalyst retained its activity for more than 24 h on stream with intermediate steps of regeneration in helium atmosphere every 4.5 h.

### 3.3.2. *Conversion in the presence of oxygen at 523 K for different HC concentrations*

The experiments in the presence of $O_2$ were performed at 523 K and a stoichiometry ratio *St*, from 0.184 to 1.05. The concentration of oxygen and the CO/NO ratio were kept constant while the $C_3^=$ concentration was changed from 13.4%$_{vol}$ to 2.5%$_{vol}$. A first remark coming out when examining the results presented in Fig. 9(a)–(c) is that in all cases examined, from net reducing to net oxidizing, an amount of $N_2O$ was found at the reactor exhaust stream due to the fact that excess oxygen consumes a significant fraction of the reducing gases that favor the $^*$–N desorption as $N_2$. In the presence of excess oxygen there are two main reaction paths, apart from the support depletion, that conclude to the production of carbon dioxide:

$$4CO + 2NO + O_2 \rightarrow 4CO_2 + N_2 \quad (10)$$

$$2C_3H_6 + 9O_2 \rightarrow 6CO_2 + 6H_2O \quad (11)$$

By examining the results presented in Table 5 and Fig. 9(a) it can be seen that when working at the higher $C_3^=$ concentration of 13.4%$_{vol}$ (lower stoichiometry ratio *St*), the presence of oxygen has not any significant effect on the efficiency of the catalyst that exhibited NO conversion factor of $R = 1$ and $N_2$ selectivity $S = 0.9$ for more than 3 h on stream. From the stoichiometry of the aforementioned oxidation reactions and the experimentally derived conversions of CO and $C_3H_6$, a consumption of 10.05%$_{vol}$ $O_2$ and a production of 8.3%$_{vol}$ $CO_2$ can be calculated. The excess oxygen consumption of 0.65%$_{vol}$ (10.05–9.4) resulted from the NO scission, while the excess $CO_2$ production of 0.7%$_{vol}$ (38.3–29.3–8.3) resulted from the support depletion.

It is interesting to note that excess oxygen consumption and excess $CO_2$ production come into convergence, a fact indicating that most of the oxygen that is produced out of the NO scission is desorbed through the support depletion according to the stoichiometry of the reaction $C_s + O_2 \rightarrow CO_2$. Lowering the $C_3^=$ to the half (6.4%$_{vol}$) had no effect on the NO conversion efficiency $R = 1$, (Fig. 9(b), Table 5), whereas the $N_2$ selectivity had dropped from 0.92 to 0.74. By applying calculations similar to these applied in the previous experiment, the excess oxygen consumption resulting from the NO scission was defined at 2.1%$_{vol}$ whereas the excess $CO_2$ production from the support depletion was 2.0%$_{vol}$. Thereby, decreasing the HC concentration resulted in higher contribution of the support to the oxygen desorption and as a consequence the NO abatement capacity remained unaffected.

Signs for deterioration of the NO abatement efficiency are given in the 3rd experiment (Fig. 9(c)) where the applied stoichiomet-

**Table 5**
Catalytic experiments in the presence of oxygen at 523 K for different HC concentrations.

| | | | | | | | |
|---|---|---|---|---|---|---|---|
| **1st test**. Fig. 9(a). Regeneration conditions: 6 h 350 °C with helium and overnight 180 °C with helium. St/GHSV/total flow-0.184/5473 $h^{-1}$/43 ml $min^{-1}$ | | | | | | | |
| | **NO** | **CO** | **$N_2$** | **$O_2$** | **$C_3$** | **$CO_2$** | **$N_2O$** |
| **Feed concentration** | 3.7 | 2.0 | 0.0 | 9.4 | 13.4 | 29.3 | 0.0 |
| | ***R*** | | ***S*** | | | | ***S*** |
| 523 K | 1 | | 0.9 | | | | 0.1 |
| **2nd test**. Fig. 9(b). Regeneration conditions: 6 h 350 °C with helium and overnight 180 °C with helium. St/GHSV/total flow-0.427/5473 $h^{-1}$/43 ml $min^{-1}$ | | | | | | | |
| | **NO** | **CO** | **$N_2$** | **$O_2$** | **$C_3$** | **$CO_2$** | **$N_2O$** |
| **Feed concentration** | 3.7 | 1.43 | 0.0 | 10.7 | 6.36 | 33.55 | 0.0 |
| | ***R*** | | ***S*** | | | | ***S*** |
| 523 K | 1 | | 0.74 | | | | 0.35 |
| **3rd test**. Fig. 9(c). Regeneration conditions: 6 h 350 °C with helium and overnight 180 °C with helium. St/GHSV/total flow-1.05/5473 $h^{-1}$/43 ml $min^{-1}$ | | | | | | | |
| | **NO** | **CO** | **$N_2$** | **$O_2$** | **$C_3$** | **$CO_2$** | **$N_2O$** |
| **Feed concentration** | 3.0 | 0.96 | 0 | 10.3 | 2.5 | 32.2 | 0 |
| | ***R*** | | ***S*** | | | | ***S*** |
| 523 K | 0.92 | | 0.42 | | | | 0.6 |

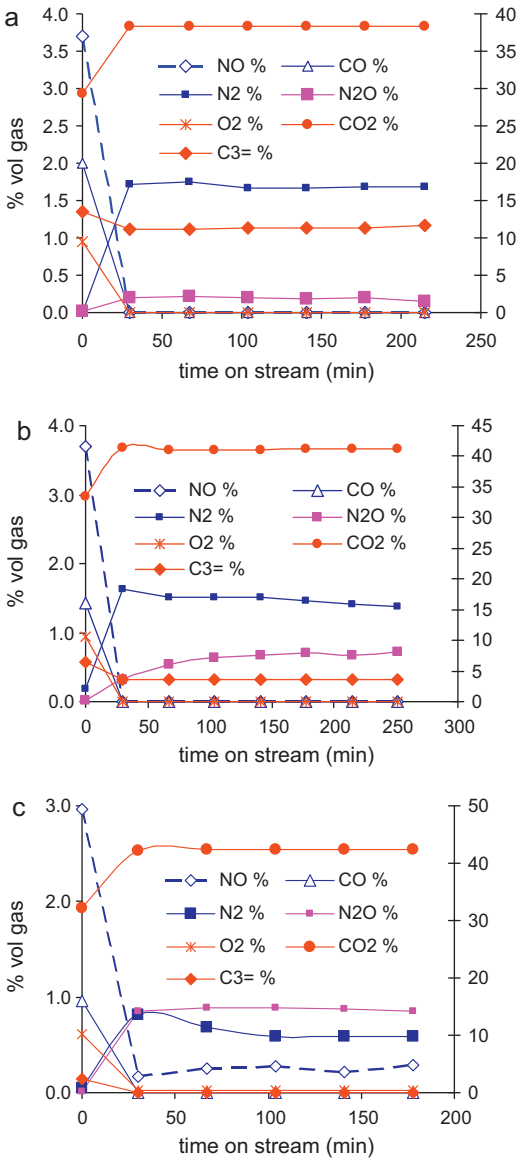


**Fig. 9.** Reactor outlet concentration at 523 K and (a) *St* = 0.184, (b) *St* = 0.427, (c) *St* = 1.05. Red symbols correspond to the secondary *y*-axis. (For interpretation of the references to color in this figure legend, the reader is referred to the web version of the article.)

ric ratio, *St*, was above 1. The conversion factor *R* drops to about 0.92 whereas the $N_2$ selectivity *S* to 0.42. The excess oxygen consumption and the excess $CO_2$ production were calculated at 1.86 and 1.85%$_{vol}$, respectively. From the experiments performed in the presence of oxygen, it can be concluded that the HC content mainly affects the selectivity of the NO conversion toward the production of nitrogen. The conversion efficiency remains unaffected whereas the support contribution to the desorption of oxygen seems to level off at stoichiometric conditions.

## 4. Conclusions

SWNT functionalization with PEG-200 led to formation of highly active Rh nanoparticles that were dispersed and adequately stabilized on the surface of the nanotubes. PEG acted as particle attachment agent, reducing medium, and agglomeration inhibitor for both nanotubes and particles. The high activity of the developed nanostructured catalyst even at low metal loadings and the significant contribution of the graphitic support were confirmed by interpreting the transient adsorption curves of the catalyst mass change upon exposure to NO at different partial pressures and temperatures. The onset temperature for oxygen desorption was defined at 383 K and NO partial pressures above 250 mbar, while similar SWNTs-supported noble metal catalyst systems start to be effective at temperatures higher than 523 K. The life cycle of the developed catalyst was investigated by NO exposure experiments at different temperatures both in the presence and absence of a reducing gas. It has been reported that a mass loss of about 9% due to the carbon support depletion at pure NO atmosphere resulted in a decrease of the NO scission capacity of the Rh nanoparticles of about 10%. In the presence of a reducing gas like CO however, the catalyst retained its activity for more than 24 h on stream with intermediate steps of regeneration in helium atmosphere every 4.5 h. Moreover, it was found that the contribution of the support to the oxygen desorption from the catalyst surface was more significant at moderate temperatures below 473 K and depended inversely on the CO/NO ratio.

## Acknowledgements

We thank Nikos Boukos and Vlassis Likodimos for assistance with TEM and Raman characterization, respectively. Financial support by the European Community through the NEXT-GTL FP7 project (grant agreement no. 229183) and the NANOTUBEMEM FP7 Marie Curie IRG project (grant agreement no. 210947) is greatly acknowledged.

## References

[1] E.A. Efthimiadis, G.D. Lionta, S.C. Christoforou, I.A. Vasalos, The effect of $CH_4$, $H_2O$ and $SO_2$ on the NO reduction with $C_3H_6$, Catal. Today 40 (1998) 15–26.

[2] W. Schießer, H. Vinek, A. Jentys, Catalytic reduction of $NO_x$ over transition-metal-containing MCM-41, Catal. Lett. 56 (1998) 189–194.
[3] K. Rahkamaa, T. Salmi, Investigation of the catalytic decomposition of NO and $N_2O$ on supported Rh with transient techniques, Chem. Eng. Sci. 54 (1999) 4343–4349.
[4] H.S. Glick, J.J. Klein, W. Squire, Single-pulse shock tube studies of the kinetics of the reaction $N_2 + O_2 \rightarrow 2NO$ between 2000–3000 K, J. Chem. Phys. 27 (1957) 850–857.
[5] L. Ilieva, G. Pantaleo, I. Ivanov, A.M. Venezia, D. Andreeva, Gold catalysts supported on $CeO_2$ and $CeO_2$–$Al_2O_3$ for $NO_x$ reduction by CO, Appl. Catal. B 65 (2006) 101–109.
[6] D. Mantri, P. Aghalayam, Detailed surface reaction mechanism for reduction of NO by CO, Catal. Today 119 (2007) 88–93.
[7] S. Mendioroz, A.B. Martín-Rojo, F. Rivera, J.C. Martín, A. Bahamonde, M. Yates, Selective catalytic reduction of $NO_x$ by methane in excess oxygen over Rh based aluminium pillared clays, Appl. Catal. B 64 (2006) 161–170.
[8] J. Pérez-Ramírez, J.M. García-Cortés, F. Kapteijn, M.J. Illán-Gómez, A. Ribera, C. Salinas-Martínez de Lecea, J.A. Moulijn, Dual-bed catalytic system for $NO_x$–$N_2O$ removal: a practical application for lean-burn deNOx HC-SCR, Appl. Catal. B 25 (2000) 191–203.
[9] J. Li, J. Hao, L. Fu, T. Zhu, High efficiency of noble metal and metal oxide catalyst systems for the selective reduction of NO with propene in lean exhaust gas, Top. Catal. 30–31 (2004) 81–84.
[10] S.I. Matsumoto, Y. Ikeda, H. Suzuki, M. Ogai, N. Miyoshi, $NO_x$ storage-reduction catalyst for automotive exhaust with improved tolerance against sulfur poisoning, Appl. Catal. B 25 (2000) 115–124.
[11] H. Abdulhamid, E. Fridell, M. Skoglundh, The reduction phase in $NO_x$ storage catalysis: effect of type of precious metal and reducing agent, Appl. Catal. B 62 (2006) 319–328.
[12] T. Lesage, C. Verrier, P. Bazin, J. Saussey, M. Daturi, Studying the NO-trap mechanism over a Pt–Rh/Ba/$Al_2O_3$ catalyst by operando FT-IR spectroscopy, Phys. Chem. Chem. Phys. 5 (2003) 4435–4440.
[13] H. Ohtsuka, The selective catalytic reduction of nitrogen oxides by methane on noble metal-loaded sulfated zirconia, Appl. Catal. B 33 (2001) 325–333.
[14] Y. Zhang, M.E. Grass, S.E. Habas, F. Tao, T. Zhang, P. Yang, G.A. Somorjai, One-step polyol synthesis and langmuir-blodgett monolayer formation of size-tunable monodisperse rhodium nanocrystals with catalytically active (1 1 1) surface structures, J. Phys. Chem. C 111 (2007) 12243–12253.
[15] G.N. Karanikolos, P. Alexandridis, T.J. Mountziaris, Growth of ZnSe and CdSe nanostructures in self-assembled block copolymer-stabilized templates, Mater. Sci. Eng. B 152 (2008) 66–71.
[16] G.N. Karanikolos, N.L. Law, R. Mallory, A. Petrou, P. Alexandridis, T.J. Mountziaris, Water-based synthesis of ZnSe nanostructures using amphiphilic block copolymer stabilized lyotropic liquid crystals as templates, Nanotechnology 17 (2006) 3121–3128.
[17] C.M. Veziri, G.N. Karanikolos, G. Pilatos, E.C. Vermisoglou, K. Giannakopoulos, C. Stogios, N.K. Kanellopoulos, Growth and morphology manipulation of carbon nanostructures on porous supports, Carbon 47 (2009) 2161–2173.
[18] M. Lepage, T. Visser, F. Soulimani, A. Iglesias-Juez, B.M. Weckhuysen, Promotion effects in the reduction of NO by CO over zeolite-supported Rh catalysts, J. Phys. Chem. C 114 (2010) 2282–2292.
[19] J. Renzas, Y. Zhang, W. Huang, G. Somorjai, Rhodium nanoparticle shape dependence in the reduction of NO by CO, Catal. Lett. 132 (2009) 317–322.
[20] L.A. Avalos, V. Bustos, R. Uñac, F. Zaera, G. Zgrablich, Dynamic Monte Carlo simulation of the NO + CO reaction on Rh(1 1 1), J. Phys. Chem. B 110 (2006) 24964–24971.
[21] J. Cortés, E. Valencia, Interpretation of the experimental data on the reduction reaction of NO by CO on rhodium by Monte Carlo simulations and by solving the kinetic equations of the reaction mechanism, J. Phys. Chem. B 110 (2006) 7887–7897.
[22] O.R. Inderwildi, S.J. Jenkins, D.A. King, Dynamic interplay between diffusion and reaction: nitrogen recombination on Rh{2 1 1} in car exhaust catalysis, J. Am. Chem. Soc. 130 (2008) 2213–2220.
[23] I. Nakai, H. Kondoh, T. Shimada, M. Nagasaka, R. Yokota, T. Katayama, K. Amemiya, H. Orita, T. Ohta, Mechanism of N + NO reaction on Rh(1 1 1) surfaces: a precursor-mediated reaction, J. Phys. Chem. C 113 (2009) 13257–13265.
[24] X. Pan, Z. Fan, W. Chen, Y. Ding, H. Luo, X. Bao, Enhanced ethanol production inside carbon-nanotube reactors containing catalytic particles, Nat. Mater. 6 (2007) 507–511.
[25] J.K. Chinthaginjala, K. Seshan, L. Lefferts, Preparation and application of carbon-nanofiber based microstructured materials as catalyst supports, Ind. Eng. Chem. Res. 46 (2007) 3968–3978.
[26] G.E. Romanos, V. Likodimos, R.R.N. Marques, T.A. Steriotis, S.K. Papageorgiou, J.L. Faria, J.L. Figueiredo, A.N.M.T. Silva, P. Falaras, Controlling and quantifying oxygen functionalities on hydrothermally and thermally treated single-wall carbon nanotubes, J. Phys. Chem. C 115 (2011) 8534–8546.
[27] G. Girishkumar, T.D. Hall, K. Vinodgopal, P.V. Kamat, Single wall carbon nanotube supports for portable direct methanol fuel cells, J. Phys. Chem. B 110 (2005) 107–114.
[28] J.Z. Luo, L.Z. Gao, Y.L. Leung, C.T. Au, The decomposition of NO on CNTs and 1 wt% Rh/CNTs, Catal. Lett. 66 (2000) 91–97.
[29] S.H. Tang, B.C. Liu, Q. Liang, L.Z. Gao, L.F. Zhang, Z.L. Yu, NO decomposition on Rh supported CNTs, Chin. Chem. Lett. 12 (2001) 83–86.
[30] H. Beyer, K. Chatziapostolou, K. Köhler, Abatement of NO using rhodium catalysts supported on carbon nanotubes: carbon as support material and reducing agent, Top. Catal. 52 (2009) 1752–1756.
[31] H. Beyer, K. Köhler, $NO_x$ removal by rhodium catalysts supported on carbon nanotubes: evidence for the stoichiometric reduction of $NO_2$ and NO by the carbon support, Appl. Catal. B 96 (2010) 110–116.
[32] T. Sakai, P. Alexandridis, Mechanism of gold metal ion reduction nanoparticle growth and size control in aqueous amphiphilic block copolymer solutions at ambient conditions, J. Phys. Chem. B 109 (2005) 7766–7777.
[33] H.W. Cooper, J.C. Goldfrank, Hydrocarbon Process. 46 (1967) 141.
[34] E.C. Vermisoglou, G.E. Romanos, V. Tzitzios, G.N. Karanikolos, V. Akylas, A. Delimitis, G. Pilatos, N.K. Kanellopoulos, Synthesis of nanocrystalline gold-carbon nanotube composites and evaluation of their sorption and catalytic properties, Micropor. Mesopor. Mater. 120 (2009) 122–131.
[35] M.S. Dresselhaus, G. Dresselhaus, R. Saito, A. Jorio, Raman spectroscopy of carbon nanotubes, Phys. Rep. 409 (2005) 47–99.
[36] T. Assmus, K. Balasubramanian, M. Burghard, K. Kern, M. Scolari, N. Fu, A. Myalitsin, A. Mews, Raman properties of gold nanoparticle-decorated individual carbon nanotubes, Appl. Phys. Lett. 90 (2007).
[37] L. Tong, Z. Li, T. Zhu, H. Xu, Z. Liu, Single gold-nanoparticle-enhanced raman scattering of individual single-walled carbon nanotubes via atomic force microscope manipulation, J. Phys. Chem. C 112 (2008) 7119–7123.
[38] M.J. Illán-Gómez, E. Raymundo-Piñero, A. García-García, A. Linares-Solano, C. Salinas-Martínez de Lecea, Catalytic $NO_x$ reduction by carbon supporting metals, Appl. Catal. B: Environ. 20 (1999) 267–275.
[39] E. Yoo, L. Gao, T. Komatsu, N. Yagai, K. Arai, T. Yamazaki, K. Matsuishi, T. Matsumoto, J. Nakamura, Atomic hydrogen storage in carbon nanotubes promoted by metal catalysts, J. Phys. Chem. B 108 (2004) 18903–18907.
[40] V.P. Zhdanov, B. Kasemo, Mechanism and kinetics of the NO–CO reaction on Rh, Surf. Sci. Rep. 29 (1997) 35–90.
[41] S. Santucci, S. Picozzi, F. Di Gregorio, L. Lozzi, C. Cantalini, L. Valentini, J.M. Kenny, B. Delley, $NO_2$ and CO gas adsorption on carbon nanotubes: experiment and theory, J. Chem. Phys. 119 (2003) 10904–10910.
[42] J. Zhao, A. Buldum, J. Han, J.P. Lu, Gas molecule adsorption in carbon nanotubes and nanotube bundles, Nanotechnology 13 (2002) 195–200.
[43] G.P. Lithoxoos, A. Labropoulos, L.D. Peristeras, N. Kanellopoulos, J. Samios, I.G. Economou, Adsorption of $N_2$, $CH_4$, CO and $CO_2$ gases in single walled carbon nanotubes: a combined experimental and Monte Carlo molecular simulation study, J. Supercritical Fluids 55 (2010) 510–523.
[44] J.-X. Zhao, Y.-H. Ding, Theoretical study of the interactions of carbon monoxide with Rh-decorated (8,0) single-walled carbon nanotubes, Mater. Chem. Phys. 110 (2008) 411–416.
[45] D.R. Kauffman, D.C. Sorescu, D.P. Schofield, B.L. Allen, K.D. Jordan, A. Star, Understanding the sensor response of metal-decorated carbon nanotubes, Nano Lett. 10 (2010) 958–963.
[46] T. Nakatsuji, T. Yamaguchi, N. Sato, H. Ohno, A selective $NO_x$ reduction on Rh-based catalysts in lean conditions using CO as a main reductant, Appl. Catal. B 85 (2008) 61–70.
[47] A. Obuchi, A. Ogata, H. Takahashi, J. Oi, G.R. Bamwenda, K. Mizuno, Selective reduction of nitrogen oxides with various organic substances on precious metal catalysts under a high GHSV condition, Catal. Today 29 (1996) 103–107.
[48] H. Shinjoh, T. Tanabe, K. Yokota, M. Sugiura, Comparative $NO_x$ reduction behavior of Pt, Pd, and Rh supported catalysts in simulated exhaust gases as a function of oxygen concentration, Top. Catal. 30–31 (2004) 319–323.